ADVANCED MATERIALS
www.advmat.de

2D $NbOI_2$: A Chiral Semiconductor with Highly In-Plane Anisotropic Electrical and Optical Properties

Yuqiang Fang, Fakun Wang, Ruiqi Wang, Tianyou Zhai, and Fuqiang Huang**

Exploring in-plane anisotropic 2D materials is of great significance to the fundamental studies and further development of polarizationsensitive optoelectronics. Herein, chiral niobium oxide diiodide ($NbOI_2$) is introduced into the intriguing anisotropic 2D family with the experimental demonstration of anisotropic optical and electrical properties. 2D $NbOI_2$ crystals exhibit highly anisotropic dispersed band structures around the Fermi surface and strong in-plane anisotropy of phonon vibrations owing to the different bonding modes of Nb atoms along the *b*- and *c*-axes. Consequently, the anisotropic factors of optical absorbance and photoresponsivity in 2D $NbOI_2$ crystals reach up to 1.75 and 1.7, respectively. These anisotropic properties make 2D $NbOI_2$ an interesting platform for novel polarization-sensitive optoelectronic applications.

1. Introduction

2D layered materials with in-plane anisotropy have attracted tremendous research interests due to their highly anisotropic band structures, rich in-plane atomic arrangements and huge potentials in polarized optoelectronic applications.[1–9] Compared with typical isotropic graphene, MoS_2, and MXenes,[10–12] emerging anisotropic 2D materials such as black phosphorus,[13–17] ReS_2,[18–20] $GeAs_2$,[21] and $PdSe_2$[22] show distinctive behavior in optical absorbance, electrical transports, and photodetection. On account of the unique anisotropic properties, such materials are designed as crystal orientation-induced diodes,[23,24] polarization-sensitive photodetectors,[25,26] synaptic-neuromorphic devices,[27] etc. Although the research on anisotropic 2D materials is progressing rapidly, it is still in its infancy as a whole. Therefore, developing new materials and exploring their anisotropic physical properties and functional devices are of great significance to the development of science and technology.

Recently, layered transition metal oxide dihalides MOX_2 (M = V, Nb, Ta, Mo; X = Cl, Br, I) have gained increasing attention among materials scientists due to their chiral crystal structure and unique physical properties.[28–33] Among them, $NbOI_2$ has a low-symmetry monoclinic structure (space group *C*2), in which Nb atoms shift away from the center of $[NbO_2I_4]$ octahedra connected by sharing I–I edges and cornered O atoms along the *c*- and *b*-axes. Various connection modes enable $NbOI_2$ strong anisotropic physical properties and highly dispersed band structure. The simulated optical absorption coefficient along the *c*-axis (α_c) is an order of magnitude higher than that along the *b*-axis (α_b).[34] Consequently, the $NbOI_2$ is expected to exhibit unique in-plane anisotropy. However, until now, the preparation and basic properties of 2D $NbOI_2$ crystals have not been thoroughly investigated, and in particular, the in-plane anisotropy caused by its low-symmetry structure is still unclear.

Here, we introduce a kind of transition metal oxide dihalides, $NbOI_2$, into the 2D materials family with experimental demonstration of strong in-plane anisotropy. Few-layer and monolayer $NbOI_2$ crystals were obtained through mechanical exfoliation, and these crystals showed large second harmonic generation (SHG) response, verifying its noncentrosymmetric crystal structure. The strong in-plane anisotropy of phonon vibration in 2D $NbOI_2$ crystals was observed by using angle-resolved polarized Raman measurements. The anisotropic electronic dispersion around the Fermi surfaces leads to the strong anisotropy of optical absorbance with an anisotropic factor of 1.75. In addition, highly anisotropic in-plane electrical resistance with a factor of 1.34 and photoresponsivity with a factor of 1.7 were demonstrated in 2D $NbOI_2$ crystals. These findings indicate that the 2D $NbOI_2$ crystal can serve as a promising candidate in anisotropic electronic and optoelectronic devices.

2. Results and Discussion

Bulk $NbOI_2$ belongs to the monoclinic space group *C*2 (No. 5) with a = 15.18 Å, b = 3.92 Å, c = 7.52 Å, β = 105.5°. **Figure 1**a

Dr. Y. Q. Fang, Prof. F. Q. Huang
State Key Laboratory of High-Performance Ceramics and Superfine Microstructure
Shanghai Institute of Ceramics
Chinese Academy of Sciences
Shanghai 200050, P. R. China
E-mail: huangfq@mail.sic.ac.cn

F. K. Wang, Prof. T. Y. Zhai
State Key Laboratory of Materials Processing and Die & Mould Technology
School of Materials Science and Engineering
Huazhong University of Science and Technology
Wuhan 430074, P. R. China
E-mail: zhaity@hust.edu.cn

Dr. R. Q. Wang, Prof. F. Q. Huang
State Key Laboratory of Rare Earth Materials Chemistry and Applications
College of Chemistry and Molecular Engineering
Peking University
Beijing 100871, P. R. China

The ORCID identification number(s) for the author(s) of this article can be found under https://doi.org/10.1002/adma.202101505.

DOI: 10.1002/adma.202101505

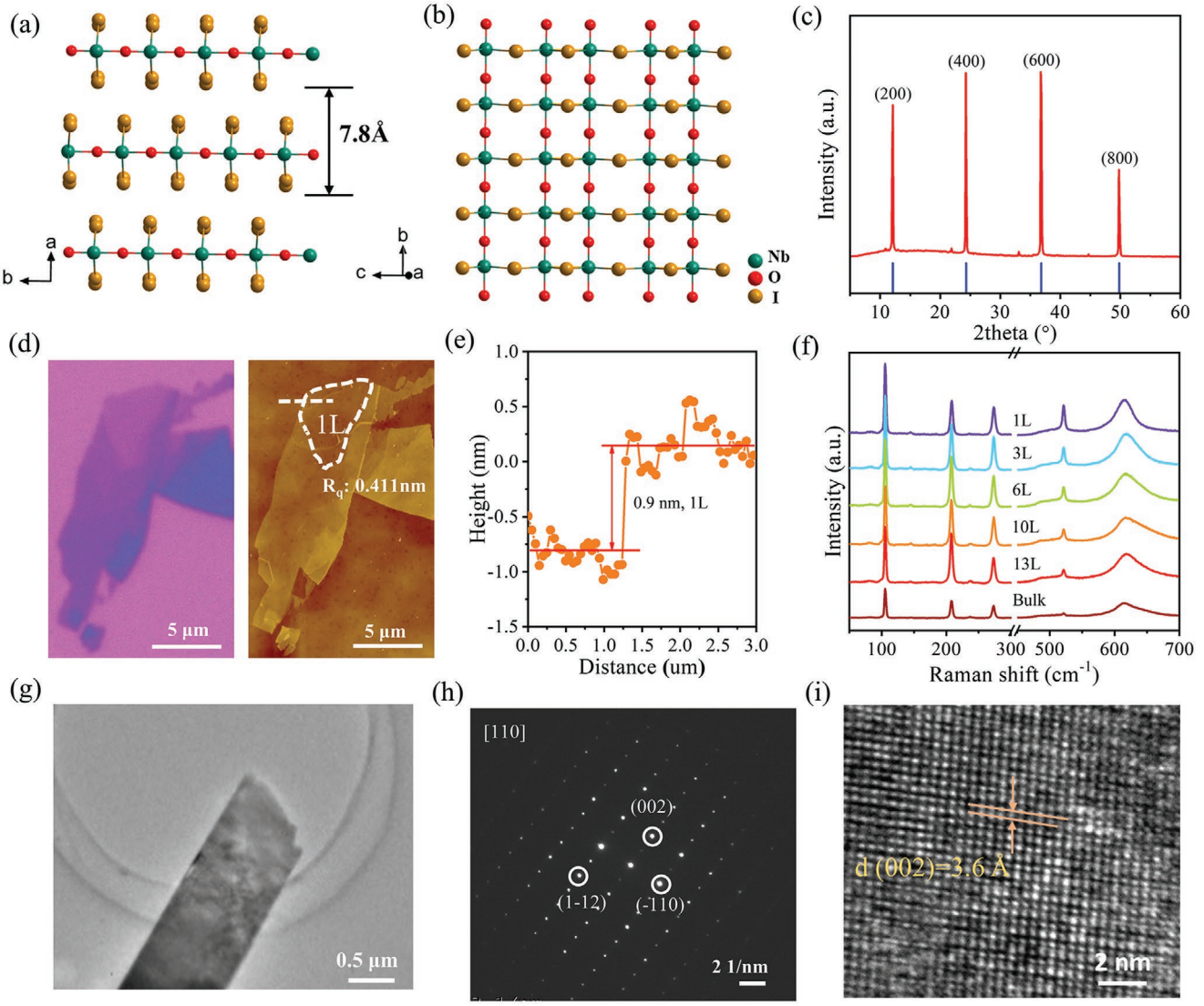

Figure 1. a,b) Schematic atomic structure of $NbOI_2$ with single layer of 7.8 Å from the *c*-axis and the *a*-axis. c) Powder X-ray pattern of the $NbOI_2$ crystals. d) OM and AFM images of as-exfoliated 2D $NbOI_2$ flake. e) The thickness of monolayer $NbOI_2$. f) Raman spectra of 2D $NbOI_2$ flakes with different thicknesses. g) Low-magnification TEM image of a typical 2D $NbOI_2$ flake. h) SAED pattern of the 2D $NbOI_2$ flake in (g). i) Low-magnification TEM image of the 2D $NbOI_2$ flake in (g).

shows that $NbOI_2$ has a typical layered structure, in which monolayer $NbOI_2$ with a thickness of 7.8 Å. Nb and O atoms form a [NbO] network grid, which is sandwiched by iodine layers. Similar to perovskite structure, $NbOI_2$ layers are constituted of $[NbO_2I_4]$ octahedra, which are connected by edge-sharing of I–I edges along the *c*-axis and by corner-sharing of O atoms along the *b*-axis. Nb atoms deviate from the center of $[NbO_2I_4]$ octahedra, forming Peierls distortion. The top view of monolayer $NbOI_2$ in Figure 1b shows rectangle network lattice. Figure S1a (Supporting Information) shows the shiny black $NbOI_2$ crystals, which were synthesized through self-vapor transport technology with Nb_2O_5, Nb, and I_2 powders as precursors. The lateral size of the as-synthesized $NbOI_2$ crystals can be up to 5–10 mm. $NbOI_2$ crystals are very stable in atmosphere, which can be confirmed by the unchanged Raman spectra after several months (Figure S1b, Supporting Information). The energy-dispersive X-ray spectroscopy spectrum (EDS) of $NbOI_2$ crystal shows a ratio of Nb, O, and I with 1:0.86:2, and elemental mapping demonstrates the uniformly distributed Nb, O, and I elements (Figure S1c–f, Supporting Information). The element fraction of oxygen deviates from 1, resulting from the inaccuracy of EDS for small atomic number. Figure 1c presents the powder X-ray diffraction of the as-synthesized $NbOI_2$ crystals. Four peaks including (200) peak at 12.1°, (400) peak at 24.3°, (600) peak at 36.8°, and (800) peak at 49.8° are confirmed, indicating the preferential growth orientation of $NbOI_2$ is (100) plane. The elemental binding energy of $NbOI_2$ crystals was examined by X-ray photoelectron spectroscopy (XPS). As shown in Figure S2a (Supporting Information), the two peaks located at 204.7 and 210.6 eV can be identified to Nb $3d_{5/2}$ and $3d_{3/2}$, the peaks at 620.2 and 631.3 eV belong to I $3d_{5/2}$ and $3d_{3/2}$, and the peak at 532.1 eV is the signal of O 1s.

Due to the weak interlayer van der Waals interaction, bulk $NbOI_2$ crystals can be peeled off several times with scotch tape. Then the exfoliated few-layer or monolayer flakes can be transferred onto the silica substrate using poly(dimethylsiloxane) (PDMS) film. Figure 1d shows the optical microscopy (OM) image and atomic force microscopy (AFM) image of mechanically exfoliated 2D $NbOI_2$ flakes on a silicon wafer with 300 nm oxidation layer. The 2D $NbOI_2$ flakes with different layers exhibit an optical contrast map depending on layer thickness. The lowest thickness of obtained $NbOI_2$ flakes is 0.9 nm, corresponding to monolayer (Figure 1e). Figure 1f shows Raman spectra of 2D $NbOI_2$ flakes with thickness ranging from bulk to 1 L. There exist five peaks (P_1–P_5 from low to high frequency) in the detecting Raman spectra range. These peaks barely changed with thickness, indicating the weak interlayer coupling of $NbOI_2$ layers. The low magnification transmission electron microscopy (TEM) image of as-exfoliated 2D $NbOI_2$ flake shows a long stripe with two parallel edges (Figure 1g), indicating a preferential cleaving orientation of $NbOI_2$ caused by its anisotropic crystal structure. Figure 1h shows the sharp selected-area electron diffraction (SAED) spots, reflecting the high crystallinity of as-exfoliated 2D $NbOI_2$ flake. The (–110), (1–12), and (002) planes are confirmed from the [110] zone axis. Subsequently, the high-resolution TEM was performed to examine the crystallinity and the relative orientation of as-exfoliated 2D $NbOI_2$ flakes. As shown in Figure 1i, the interplanar length vertical to the edge is 3.6 Å corresponding to the (002) plane, which indicates the long side direction is [002]. Hence, the preferential cleaving orientation of $NbOI_2$ crystals is the *c*-axis, because the bonding interaction of Nb—I bonds along the *c*-axis is weaker than that of edge-sharing octahedron Nb—O bonds along the *b*-axis.

Raman spectrum contains abundant information of crystal structural orientation and phonon vibration. The phonon vibration of $NbOI_2$ should be anisotropic due to its noncentrosymmetric space group *C*2. Here, the angle-resolved polarized Raman spectroscopy (ARPRS) was performed to investigate the phonon vibrational anisotropy of $NbOI_2$. The polarized Raman scattering signals parallel and perpendicular to the polarized direction of the incident laser were collected through rotating a linear polarizer in front of the Raman detector. Figure S3 (Supporting Information) shows the Raman spectra of a 2D $NbOI_2$ flake measured in the parallel and perpendicular polarization configuration. The Raman modes P_1, P_2, P_3, P_5, and P_4 demonstrate A_g-like and B_g-like vibrations, respectively. **Figure 2**a,b presents the false-color image of the normalized polarized Raman peak intensities with the rotation angle from 0° to 360°. As shown in Figure 2a, P_1, P_2, P_3, and P_5 peaks exhibit 2-lobed shape and P_4 shows 4-lobed shape in parallel polarization configuration. While all peaks exhibit 4-lobed shape in perpendicular polarization configuration (Figure 2b). These results truly indicate that the polarized Raman intensities of $NbOI_2$ are dependent on the crystal structural orientation.

The intensity of Raman modes can be described by the equation $I \propto |e_i \mathbf{R} e_s|^2$,[35,36] in which e_i, e_s, and **R** represent the polarization vectors of incident light, scattered light, and the Raman tensor, respectively. The unit polarization vector is $e_i = (0, \cos\theta, \sin\theta)$, in which θ is the angle between the incident light and the

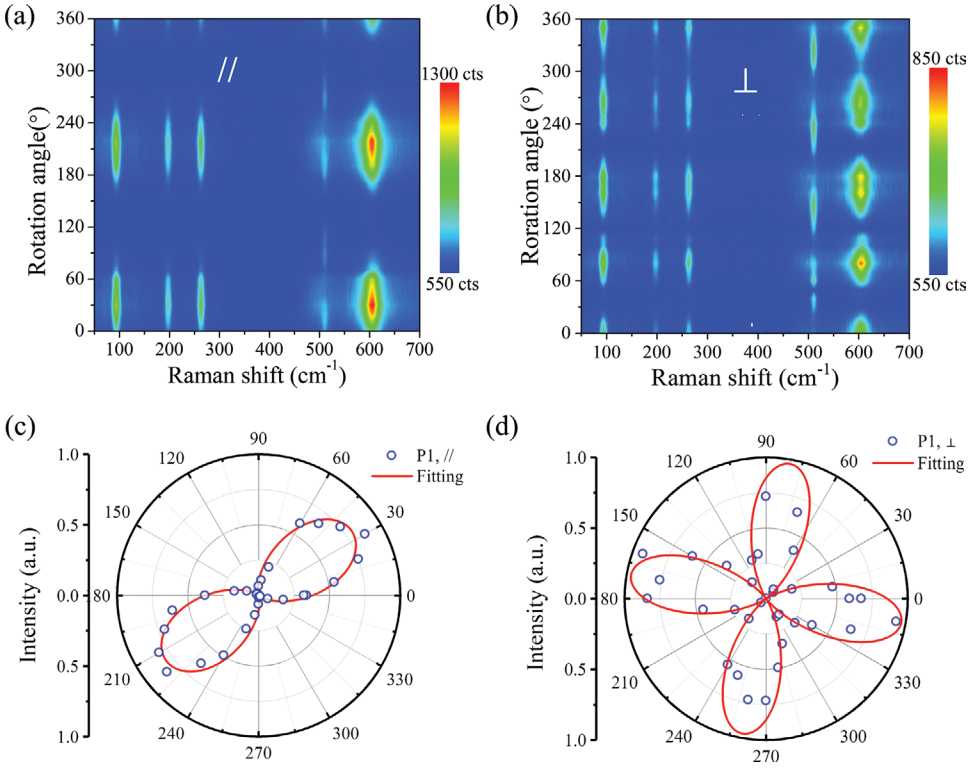

Figure 2. a,b) False-color plot of polarized Raman intensities for a 2D $NbOI_2$ flake measured in parallel and perpendicular polarization configurations. c,d) Polar plots of the measured and fitted Raman peak intensities of the P_1 peak in parallel and perpendicular polarization configurations.

b-axis of the measured 2D $NbOI_2$ flake, while e_s can be described as $e_s = (0, \cos\theta, \sin\theta)$ and $e_s = (0, -\sin\theta, \cos\theta)$ in the parallel and perpendicular configurations, respectively. Since $NbOI_2$ crystallizes in *C*2 space group, the Raman tensor can be written as

$$\mathbf{R}(A_g) = \begin{pmatrix} a & d & 0 \\ d & b & 0 \\ 0 & 0 & c \end{pmatrix} \quad (1)$$

$$\mathbf{R}(B_g) = \begin{pmatrix} 0 & 0 & e \\ 0 & 0 & f \\ e & f & 0 \end{pmatrix} \quad (2)$$

Hence, the anisotropy of Raman scattering intensities in the parallel and perpendicular polarization configurations can be expressed by the following equations[37]

$$\mathbf{I}(A,\parallel) \propto (b\cos\theta)^2 + (c\sin\theta)^2 \quad (3)$$

$$\mathbf{I}(B,\parallel) \propto (\sin 2\theta)^2 \quad (4)$$

$$\mathbf{I}(A,\perp) \propto (\sin 2\theta)^2 \quad (5)$$

$$\mathbf{I}(B,\perp) \propto (\cos 2\theta)^2 \quad (6)$$

Figure 2c,d shows the polar plot of P_1 Raman position in parallel and perpendicular polarization configuration, in which the blue dots are experimental values and the red lines represent the fitting result based on the above equations. The other four peaks are summarized in Table S1 (Supporting Information). The A_g-like modes (P_1, P_2, P_3, and P_5) exhibit 2-lobed and 4-lobed shape in the parallel and perpendicular polarization configuration, respectively. The B_g-like mode P_4 shows 4-lobed formation under the parallel and perpendicular polarization configuration. Interestingly, the A_g-like modes show maximum intensities along the *c*-axis in the parallel configuration, which is helpful for us to judge the axial direction of the 2D $NbOI_2$ flakes.

In order to investigate the interlayer thermal expansion and atomic vibration of 2D $NbOI_2$ flake, the temperature-dependent Raman characterization was performed on the 2D $NbOI_2$ flake at temperatures from 80 to 300 K.[38–41] As shown in **Figure 3**a, the intensity of observed Raman peaks increases with decreasing temperature owing to the enhanced anharmonic

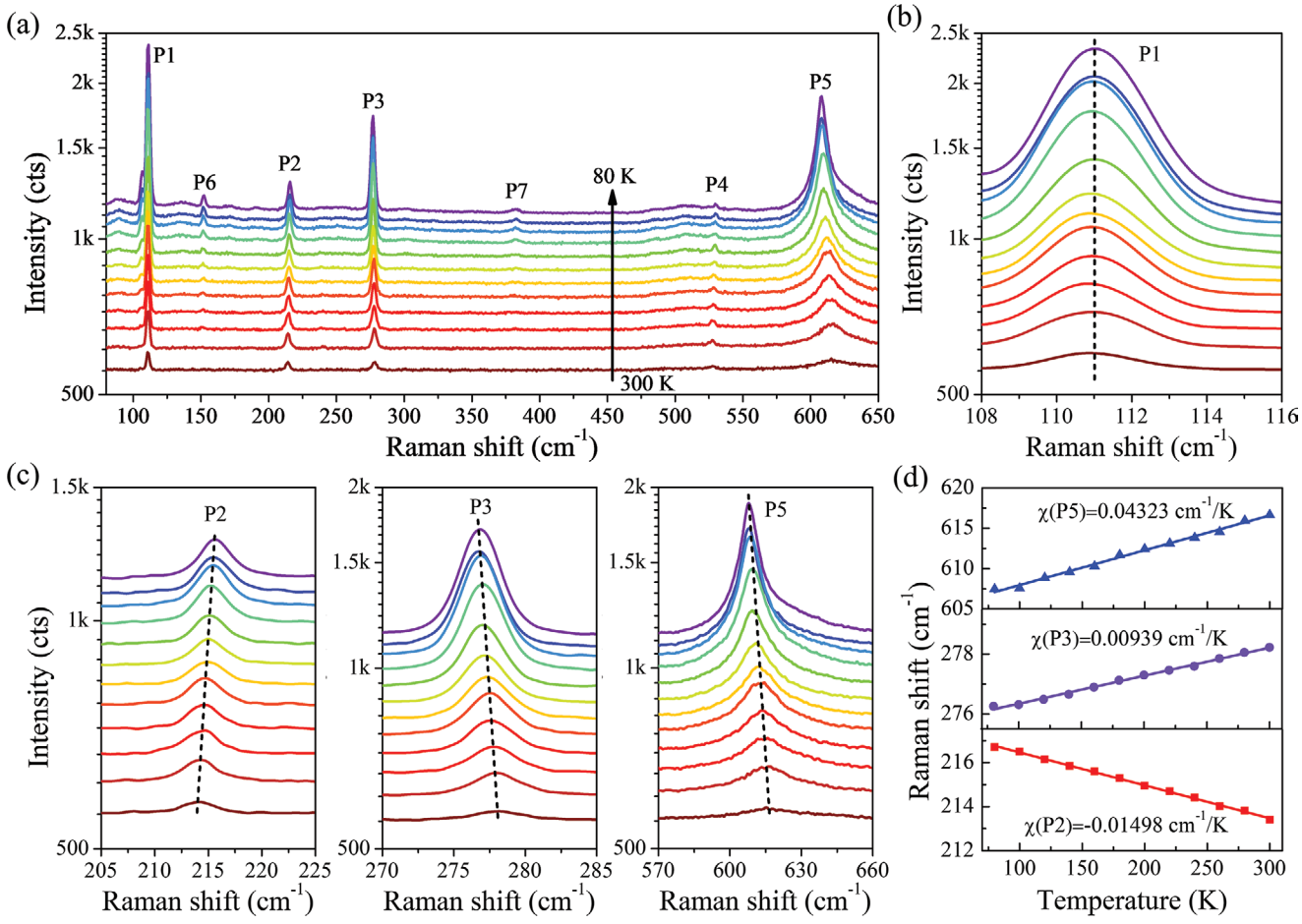

Figure 3. a) Raman spectra of 2D $NbOI_2$ flake measured at different temperature ranging from 80 to 300 K. b,c) The enlarged view of offset in the P_1–P_5 peaks at different temperature. d) Raman peak positions of P_3, P_4, and P_5 as a function of temperature.

coupling of A_g and B_g modes at higher temperature. Such coupling interaction would costume energy and decrease the thermal vibrational excitation. Figure 3b,c shows the movement of Raman peaks at temperature from 80 to 300 K. The P_1 and P_4 peaks do not shift with decreasing temperature, P_2 exhibits a redshift with decreasing temperature, which results from anharmonic lattice vibrations at higher temperature. Figure 3c presents the typical plots for Raman peak positions as a function of temperature. The temperature dependence of peak positions can be fitted by linear equation of $\omega(T) = \omega_0 + \chi(T)$, where ω_0 presents the Raman peak position at 0 K and χ is the slope of the fitted line, also indicating the first-order temperature coefficient of the related Raman modes. The χ values of P_2, P_3, and P_5 are calculated to be 0.01498, 0.00939, and 0.04323 cm^{-1} K^{-1}, respectively. The P_5 Raman mode is the most sensitive to the temperature among these three peaks. The temperature coefficient χ of $NbOI_2$ is bigger than that of $SnSe_2$, RhI_3, and graphene.[42] The value of the first-order temperature coefficient of Raman modes is proportional to the interlayer forces in the layered materials. Hence, $NbOI_2$ has stronger interlayer interaction than graphene.

Nonlinear optical effect is one of the most important properties in investigating the noncentrosymmetric materials. Since $NbOI_2$ belongs to *C*2 space group with broken inversion symmetry, SHG was measured on a 2D $NbOI_2$ flake to investigate the related nonlinear optical phenomena. **Figure 4**a shows the strong SHG response of a 2D $NbOI_2$ flake under various excitation wavelengths ranging from 800 to 1300 nm. This wavelength response region makes $NbOI_2$ crystals a potential application in infrared nonlinear optics. Figure 4b presents power dependence of SHG intensities under excitation with a wavelength of 800 nm. The wavelength of the generated laser is 400 nm, which is a half of the incident wavelength. Figure 4c displays the SHG intensities in logarithmic coordinate as a function of excitation power. The slope of the fitted plot is 1.8, which is close to the theoretically calculated value of 2, indicating that the collected signals stem from the contribution of SHG. In order to calculate the value of SHG conversion efficiency η of $NbOI_2$ flakes, monolayer MoS_2 was employed as a reference. The SHG intensities of monolayer MoS_2 and 2D $NbOI_2$ flake are shown in Figure 4d. The refractive index of $NbOI_2$ is 2.6 at 1200 nm and 2.2 at 600 nm (Figure 4e). The SHG efficiency of $NbOI_2$ is calculated to be $191\eta_{MoS_2}$ (≈19.1%), by comparing the coefficients of $NbOI_2$ flake and monolayer MoS_2 in the equation $\eta = P_{2\omega}/P_{\omega} = [8\pi^2 d^2(\chi^{(2)})^2 P_{\omega}]/[n_{\omega}{}^2 n_{2\omega}\lambda\omega^2 c\varepsilon_0]$.[43] To detect the crystal symmetry of $NbOI_2$, the polarization resolved SHG measurements were performed with the emission field parallel to the excitation field. Figure 4f displays two asymmetric lobes, resulting from the chiral symmetric space group *C*2 of $NbOI_2$ crystals. The chiral structure of $NbOI_2$ crystal was demonstrated by circular dichroism (CD) investigation (Figure S4, Supporting Information).

To determine the bandgaps of 2D $NbOI_2$ flakes with different thicknesses, the micro-optical absorption measurement was carried out in the wavelengths ranging from 300 to 900 nm. **Figure 5**a shows the absorption spectra of 2D $NbOI_2$

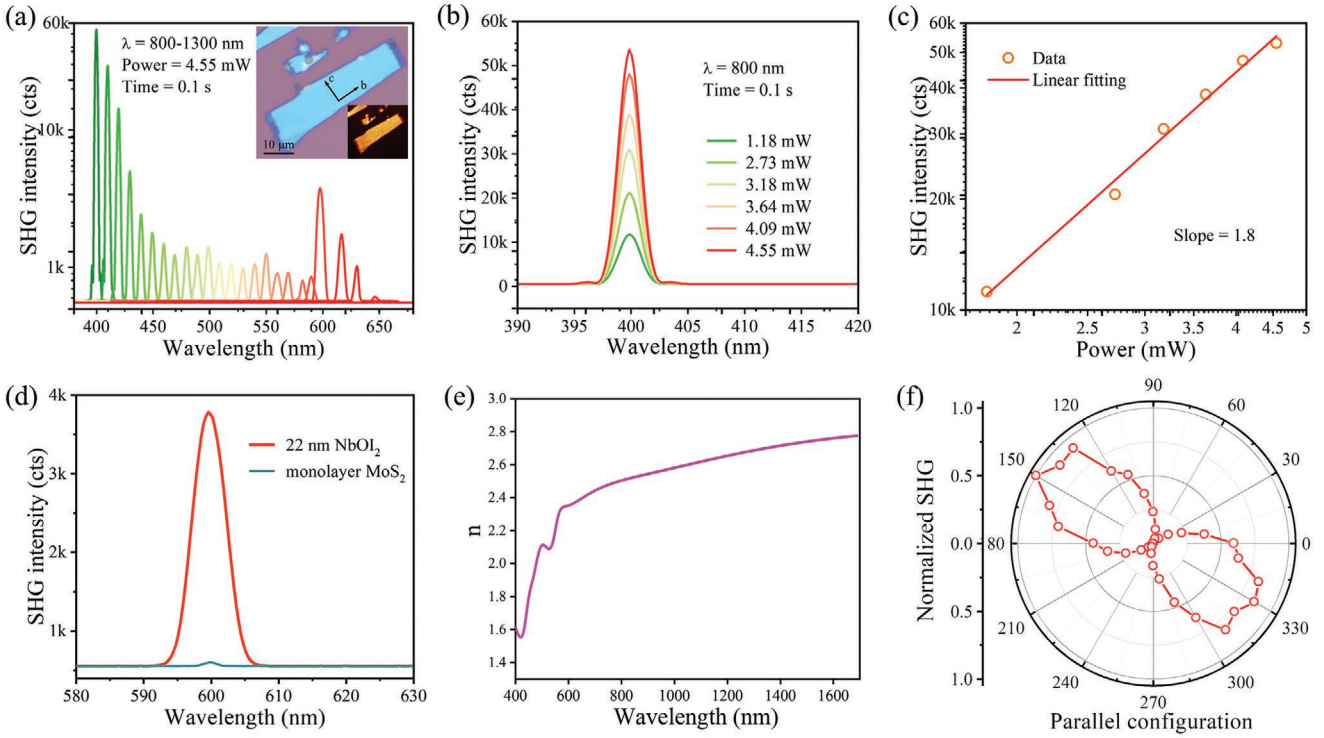

Figure 4. a) SHG signals of a 2D $NbOI_2$ flake under various excitation wavelengths ranging from 800 to 1300 nm. Inset: OM image of $NbOI_2$ flake. b) SHG spectra in the incident light of 800 nm with different powders from 1.18 to 4.55 mW. c) Powder-dependent SHG intensities. d) The SHG intensities of a 22 nm $NbOI_2$ flake and monolayer MoS_2. e) Refractive index of $NbOI_2$ at the wavelengths from 400 to 1700 nm. f) Polarization dependence of SHG intensity in parallel polarization configuration.

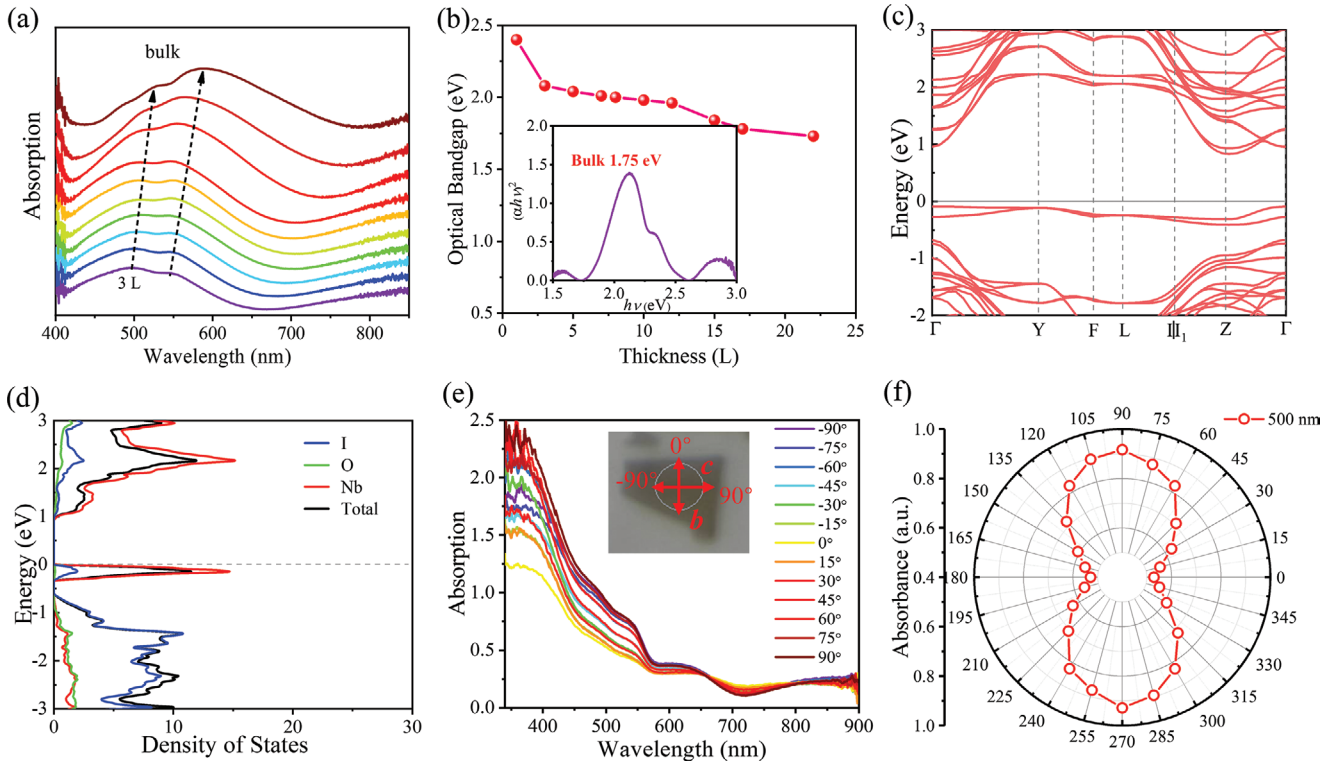

Figure 5. a) Optical absorption of 2D $NbOI_2$ flakes with different thicknesses. b) The thickness dependence of optical bandgaps of 2D $NbOI_2$ flakes. c,d) Calculated electronic band structure and density of state of bulk $NbOI_2$. e) Polarization-resolved absorption spectra of $NbOI_2$ crystal measured at the wavelength ranging from 300 to 900 nm. Inset: OM image of the sample. The measured angle rotates from −90° to 90° with steps of 15°. f) Polar plots of the absorption at wavelengths of 500 nm.

flakes with various thickness, which is confirmed by the AFM results (Figure S5, Supporting Information). The absorbance edges show a blueshift and the absorption intensities drop gradually with the decrease of thickness, suggesting the increscent bandgap resulting from quantum size effect. The specific bandgaps were determined from the spectra using Tauc plots, as presented in Figure S6 (Supporting Information). Figure 5b displays the thickness-dependent optical bandgaps of 2D $NbOI_2$ flakes, revealing the tunability of bandgap from 1.7 eV of bulk to 2.4 eV of monolayer. In addition, photoluminescence (PL) spectra of the 2D $NbOI_2$ flakes show prominent peaks at ≈2.25 eV (Figure S7, Supporting Information), which is in accordance with the optical bandgaps. The band structure and density of state of bulk $NbOI_2$ are calculated based on the DFT method (Figure 5c,d). The conduction band of $NbOI_2$ is mainly composed of the Nb-4d states, and the highest valence band below the Fermi level is mostly contributed by electrons from the I-5p and Nb-4d orbitals. Hence, the electron transition prefers to occur along the *c*-axis with I–I connection.

$NbOI_2$ reveals a great potential to detect polarized light signals owing to the in-plane anisotropic dispersed band structure. In order to understand the anisotropic features of the linear dichroism (LD) in 2D $NbOI_2$ flakes, the polarization-resolved absorption spectra were collected with polarization angle in steps of 15°, as shown in Figure 5e. The polar absorbance intensities were plotted at a wavelength of 500 nm (Figure 5f), showing a two-lobed shape, which is in accordance with the structural anisotropy. The corresponding anisotropic absorption ratio at 500 nm is calculated to be 1.75, which is larger than 1.15 and 1.09 of 2D $PdSe_2$ and GeSe flakes.[22,44] Interestingly, the dominating polarization orientation is along the *c*-axis in the visible range, while the polarization is along the *b*-axis in the near-infrared wavelength (Figure S8, Supporting Information). This phenomenon reveals that 2D $NbOI_2$ flakes exhibit wavelength-selective absorbance along various lattice axis.

Apart from anisotropic optical absorbance, the anisotropic electrical transport has been systematically studied. **Figure 6**a schematically illustrates the device with twelve electrodes in step of 30°, where the *b*-axis is defined as 0°. The optical image of the $NbOI_2$ device is shown in the inset of Figure 6a. The linear current-voltage curves at different angles reveal good Ohmic contact and the resistance of $NbOI_2$ is clearly angle-dependent. Figure 6c presents the angle-dependent resistance extracted from the data of Figure 6b. The anisotropic resistance ratio of the $NbOI_2$ device is about 1.34, slightly lower than 1.52, 1.41, and 1.8 of GeP, Ta_2NiS_5, and $GeAs_2$.[21,45] The in-plane anisotropic resistance may result from the different electronegativity between I and O atoms. The valence bands near the Fermi level of $NbOI_2$ are mainly composed of electrons from I-p orbitals. Additionally, the conduction and valence bands reveal anisotropic dispersion, and the valence and conduction bands around the Fermi surface are almost dispersed along the crystallographic *b*-axis.[34] Therefore, the electrons would migrate more easily along the *b*-axis because there exist more electrons in this direction. According to the anisotropy in electrical transport of 2D $NbOI_2$ flake, angle-resolved electrical

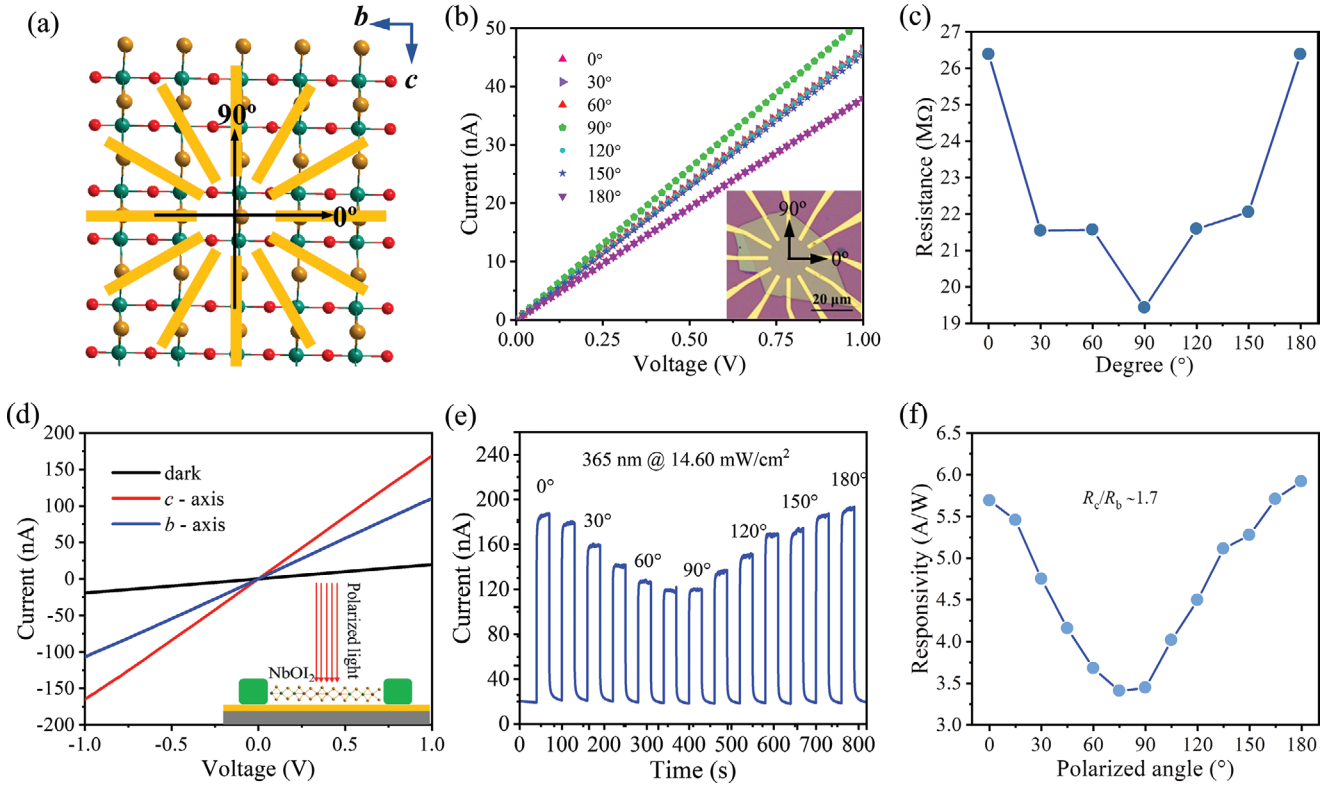

Figure 6. a) Schematic diagram of electrode structure with six pairs spaced at 30° apart. b) Current–voltage curves at different angles and the reference electrode along the *b*-axis as 0°. Inset: OM image of the $NbOI_2$ device with the labeled *b*- and *c*-axes. c) The angle-dependent resistance of 2D $NbOI_2$ flake. d) Typical current–voltage curves under dark and with light polarization orientation along the *b*- and *c*-axes. e,f) The measured photocurrent and responsivity and anisotropic factor at the angle ranging from 0° to 180° at the wavelength of 365 nm.

resistance measurements can be used to determine its in-plane structural orientation.

The strong in-plane anisotropy of electrical transport and LD conversion grant 2D $NbOI_2$ flake a potential application in polarization-sensitive photodetector. The OM and AFM images of 2D $NbOI_2$ flake reveal that the thickness of the device is 23 nm (Figure S9, Supporting Information). Figure 6d shows the typical current–voltage curves under dark and with polarized illumination along the *b*- and *c*-axes. It is obvious that the photoresponsivity at the *c*-axis is larger. The angle-resolved photoresponsivity measured at polarized angle from 0° to 180° indicates stronger On and Off current along the *c*-axis than the *b*-axis (Figure 6e). The polarized-angle-dependent responsivity is shown in Figure 6f. The value of R_c/R_b is 1.7 for the 2D $NbOI_2$ flake, which is comparable to 1.83, 2.2, 2.0, and 2.1 of 2D GeP, $PdSe_2$, $GeAs_2$, and GeS_2 flakes, respectively.[46–48] After exposure to the atmosphere for four months, the in-plane anisotropic photoresponsivity of the device remains unchanged, indicating its long-term stability (Figure S10, Supporting Information). The anisotropy factor of photoresponsivity of 2D $NbOI_2$ flake is larger than that of resistance. Hence, the polarized photodetection mainly results from the stronger optical absorption along the *c*-axis than the *b*-axis, which demonstrates that 2D $NbOI_2$ flake can be developed to be polarized optoelectronic devices. In addition, 2D $NbOI_2$ flake shows photoresponse at the wavelengths ranging from 300 to 700 nm (Figure S11, Supporting Information), demonstrating the potential application of broadband photodetection. Figure S12 (Supporting Information) shows the current–voltage curves at various excitation intensities, the fitted photocurrent (I) and responsivity (R) as a function of power density follows a power law of $I \approx P^{0.54}$ and $R \approx P^{0.46}$. The low indexes result from the trap states produced by the defects of $NbOI_2$ device. In addition, the defect trap state leads to the long response time (3 s) and relaxation time (4 s) of the device.[49] We expect that the response rate can be improved by improving the crystalline quality of 2D $NbOI_2$ flakes, constructing van der Waals heterojunctions or using surface modification methods.

3. Conclusions

We have successfully prepared 2D $NbOI_2$ crystal and investigated its in-plane anisotropic properties. ARPRS measurements reveal the large anisotropy of phonon vibration modes. Microabsorbance indicates the bandgaps of $NbOI_2$ are from 1.7 eV (bulk) to 2.4 eV (monolayer). Moreover, the angle-resolved electrical resistance and photoelectric detection indicate that the anisotropy factor of electrical conductance and photoresponsivity is 1.34 and 1.7, respectively. The in-plane anisotropic optical and electrical properties make $NbOI_2$ a promising candidate for polarization-sensitive photodetector, synaptic transistors, polarization field-effect transistors, and sensors.[50–53] In addition, due to the chirality and polarity of $NbOI_2$, it has broad

application prospects in 2D anisotropic piezoelectric and ferroelectric devices, chiral optical effect, and asymmetric catalysis.

4. Experimental Section

Sample Preparation: High-purity $NbOI_2$ single crystals were grown through a CVT method. The starting reactants Nb, Nb_2O_5 and I_2 powders in a ratio of 3:1:6 were sealed in an evacuated quartz tube. The tubes were slowly heated up to 700 °C, kept at this temperature for 3 d and cooled to room temperature with the furnace cooling naturally. The products were soaked in alcohol to remove the excess I_2. The harvested crystals were shiny rectangle plates with dimensions of $6 \times 8 \times 0.5$ mm^3. The thin $NbOI_2$ flakes were exfoliated mechanically and transferred onto a SiO_2/Si substrate. The thickness of the 2D $NbOI_2$ flakes can be confirmed through an optical microscope (Olympus, BX51) and AFM microscopy (Bruker Dimension Fast Scan).

Characterization: The PXRD patterns were measured using a Rigaku-TTR3 X-ray diffractometer with Cu-Kα target at the angle of 5°–60°. The element compositions of $NbOI_2$ crystal were confirmed through energy dispersive X-ray spectroscopy. The microstructure of the exfoliated 2D $NbOI_2$ flakes was studied by the high-resolution transmission electron microscopy (JEM-ARM2100F). The temperature-dependent Raman and angle polarization Raman spectra measurements were carried out on a microscope spectrometer, equipped with ×100 optical objective and 1800 grooves mm^{-1} grating. The excitation power and wavelength were 1 mW and 532 nm, respectively. To detect the polarized Raman spectra, the incident laser was polarized, and the scattering light was in the direction parallel and perpendicular to the incident light. The SHG signals were collected in a chameleon femtosecond laser (140 fs, 80 MHz). The optical bandgaps of 2D $NbOI_2$ flakes with different thicknesses were determined by Jasco MSV-5200 microscopic spectrophotometer.

Device Fabrication and Measurements: The devices based on 2D $NbOI_2$ flakes were fabricated by using electron-beam lithography (FEI Quanta 650 SEM and Raith Elphy Plus) and the In/Au contact electrodes produced by the thermal evaporation (Nexdep, Angstrom Engineering). The electrical transports of 2D $NbOI_2$ flakes were performed in a probe station. The angle polarization-resolved photodetection was measured by rotating the angle of polarized laser at 365 nm with a polarizer and a half-wave plate.

Supporting Information

Supporting Information is available from the Wiley Online Library or from the author.

Acknowledgements

Y.F. and F.W. contributed equally to this work. This work was supported financially by the National Natural Science Foundation of China (Grant No. 21825103), the Research Program of the Chinese Academy of Sciences (Grant No. E01YQZ18), and the Shanghai Super Postdoctoral (Grant No. E01SCB19).

Conflict of Interest

The authors declare no conflict of interest.

Data Availability Statement

The data that support the findings of this study are available from the corresponding author upon reasonable request.

Keywords

chiral 2D materials, in-plane anisotropy, $NbOI_2$

Received: February 22, 2021
Revised: April 5, 2021
Published online: June 6, 2021

[1] H. Liu, A. T. Neal, Z. Zhu, Z. Luo, X. Xu, D. Tománek, P. D. Ye, *ACS Nano* **2014**, *8*, 4033.
[2] Z. Luo, J. Maassen, Y. Deng, Y. Du, R. P. Garrelts, M. S. Lundstrom, P. D. Ye, X. Xu, *Nat. Commun.* **2015**, *6*, 8572.
[3] X. Wang, A. M. Jones, K. L. Seyler, V. Tran, Y. Jia, H. Zhao, H. Wang, L. Yang, X. Xu, F. Xia, *Nat. Nanotechnol.* **2015**, *10*, 517.
[4] N. Mao, J. Tang, L. Xie, J. Wu, B. Han, J. Lin, S. Deng, W. Ji, H. Xu, K. Liu, L. Tong, J. Zhang, *J. Am. Chem. Soc.* **2016**, *138*, 300.
[5] F. Xia, H. Wang, Y. Jia, *Nat. Commun.* **2014**, *5*, 4458.
[6] J. Tao, W. Shen, S. Wu, L. Liu, Z. Feng, C. Wang, C. Hu, P. Yao, H. Zhang, W. Pang, X. Duan, J. Liu, C. Zhou, D. Zhang, *ACS Nano* **2015**, *9*, 11362.
[7] J. Wu, N. Mao, L. Xie, H. Xu, J. Zhang, *Angew. Chem., Int. Ed.* **2015**, *54*, 2366.
[8] X. Duan, C. Wang, A. Pan, R. Yu, X. Duan, *Chem. Soc. Rev.* **2015**, *44*, 8859.
[9] W. Huang, L. Gan, H. Yang, N. Zhou, R. Wang, W. Wu, H. Li, Y. Ma, H. Zeng, T. Zhai, *Adv. Funct. Mater.* **2017**, *27*, 1702448.
[10] J. Pei, J. Yang, T. Yildirim, H. Zhang, Y. Lu, *Adv. Mater.* **2019**, *31*, 1706945.
[11] Z. Huang, W. Han, H. Tang, L. Ren, D. S. Chander, X. Qi, H. Zhang, *2D Mater.* **2015**, *2*, 035011.
[12] X. Jiang, A. V. Kuklin, A. Baev, Y. Ge, H. Ågren, H. Zhang, P. N. Prasad, *Phys. Rep.* **2020**, *848*, 1.
[13] S. Guo, Y. Zhang, Y. Ge, S. Zhang, H. Zeng, H. Zhang, *Adv. Mater.* **2019**, *31*, 1902352.
[14] S. Zhang, J. Yang, R. Xu, F. Wang, W. Li, M. Ghufran, Y.-W. Zhang, Z. Yu, G. Zhang, Q. Qin, Y. Lu, *ACS Nano* **2014**, *8*, 9590.
[15] X. Ling, S. Huang, E. H. Hasdeo, L. Liang, W. M. Parkin, Y. Tatsumi, A. R. T. Nugraha, A. A. Puretzky, P. M. Das, B. G. Sumpter, D. B. Geohegan, J. Kong, R. Saito, M. Drndic, V. Meunier, M. S. Dresselhaus, *Nano Lett.* **2016**, *16*, 2260.
[16] Q. Guo, A. Pospischil, M. Bhuiyan, H. Jiang, H. Tian, D. Farmer, B. Deng, C. Li, S. J. Han, H. Wang, Q. Xia, T. P. Ma, T. Mueller, F. Xia, *Nano Lett.* **2016**, *16*, 4648.
[17] H. Jang, J. D. Wood, C. R. Ryder, M. C. Hersam, D. G. Cahill, *Adv. Mater.* **2015**, *27*, 8017.
[18] E. Zhang, P. Wang, Z. Li, H. Wang, C. Song, C. Huang, Z. G. Chen, L. Yang, K. Zhang, S. Lu, W. Wang, S. Liu, H. Fang, X. Zhou, H. Yan, J. Zou, X. Wan, P. Zhou, W. Hu, F. Xiu, *ACS Nano* **2016**, *10*, 8067.
[19] M. Hafeez, L. Gan, H. Li, Y. Ma, T. Zhai, *Adv. Mater.* **2016**, *28*, 8296.
[20] E. Liu, Y. Fu, Y. Wang, Y. Feng, H. Liu, X. Wan, W. Zhou, B. Wang, L. Shao, C. H. Ho, Y. S. Huang, Z. Cao, L. Wang, A. Li, J. Zeng, F. Song, X. Wang, Y. Shi, H. Yuan, H. Y. Hwang, Y. Cui, F. Miao, D. Xing, *Nat. Commun.* **2015**, *6*, 6991.
[21] L. Li, P. Gong, D. Sheng, S. Wang, W. Wang, X. Zhu, X. Shi, F. Wang, W. Han, S. Yang, K. Liu, H. Li, T. Zhai, *Adv. Mater.* **2018**, *30*, 1804541.
[22] L. S. Lu, G. H. Chen, H. Y. Cheng, C. P. Chuu, K. C. Lu, C. H. Chen, M. Y. Lu, T. H. Chuang, D. H. Wei, W. C. Chueh, W. B. Jian, M. Y. Li, Y. M. Chang, L. J. Li, W. H. Chang, *ACS Nano* **2020**, *14*, 4963.
[23] H. Wang, X. Wang, F. Xia, L. Wang, H. Jiang, Q. Xia, M. L. Chin, M. Dubey, S. J. Han, *Nano Lett.* **2014**, *14*, 6424.
[24] W. Xin, X. K. Li, X. L. He, B. W. Su, X. Q. Jiang, K. X. Huang, X. F. Zhou, Z. B. Liu, J. G. Tian, *Adv. Mater.* **2018**, *30*, 1704653.

[25] F. Liu, S. Zheng, X. He, A. Chaturvedi, J. He, W. L. Chow, T. R. Mion, X. Wang, J. Zhou, Q. Fu, H. J. Fan, B. K. Tay, L. Song, R. H. He, C. Kloc, P. M. Ajayan, Z. Liu, *Adv. Funct. Mater.* **2016**, *26*, 1169.
[26] L. Ye, P. Wang, W. Luo, F. Gong, L. Liao, T. Liu, L. Tong, J. Zang, J. Xu, W. Hu, *Nano Energy* **2017**, *37*, 53.
[27] H. Tian, Q. Guo, Y. Xie, H. Zhao, C. Li, J. J. Cha, F. Xia, H. Wang, *Adv. Mater.* **2016**, *28*, 4991.
[28] J. Beck, C. Kusterer, *Z. Anorg. Allg. Chem.* **2006**, *632*, 2193.
[29] J. Rijnsdorp, F. Jellinek, *J. Less-Common Met.* **1978**, *61*, 79.
[30] M. Ruck, *Acta Crystallogr., Sect. C: Struct. Chem.* **1995**, *51*, 1960.
[31] J. Zhao, W. Wu, J. Zhu, Y. Lu, B. Xiang, S. A. Yang, *Phys. Rev. B* **2020**, *102*, 245419.
[32] M. Bortoluzzi, E. Ferretti, F. Marchetti, G. Pampaloni, C. Pinzino, S. Zacchini, *Inorg. Chem.* **2016**, *55*, 4173.
[33] H. Ai, X. Song, S. Qi, W. Li, M. Zhao, *Nanoscale* **2019**, *11*, 1103.
[34] Y. Jia, M. Zhao, G. Gou, X. C. Zeng, J. Li, *Nanoscale Horiz.* **2019**, *4*, 1113.
[35] Y. Peter, M. Cardona, *Fundamentals of Semiconductors: Physics and Materials Poperties*, Springer Science & Business Media, Berlin, Germany **2010**.
[36] L. Li, P. Gong, W. Wang, B. Deng, L. Pi, J. Yu, X. Zhou, X. Shi, H. Li, T. Zhai, *ACS Nano* **2017**, *11*, 10264.
[37] H. B. Ribeiro, M. A. Pimenta, C. J. S. de Matos, R. L. Moreira, A. S. Rodin, J. D. Zapata, E. A. T. de Souza, A. H. Castro Neto, *ACS Nano* **2015**, *9*, 4270.
[38] I. Calizo, A. A. Balandin, W. Bao, F. Miao, C. N. Lau, *Nano Lett.* **2007**, *7*, 2645.
[39] R. Yan, J. R. Simpson, S. Bertolazzi, J. Brivio, M. Watson, X. Wu, A. Kis, T. Luo, A. R. Hight Walker, H. G. Xing, *ACS Nano* **2014**, *8*, 986.
[40] J. Xia, X. Z. Li, X. Huang, N. Mao, D. D. Zhu, L. Wang, H. Xu, X. M. Meng, *Nanoscale* **2016**, *8*, 2063.
[41] S. Luo, X. Qi, H. Yao, X. Ren, Q. Chen, J. Zhong, *J. Phys. Chem. C* **2017**, *121*, 4674.
[42] F. Wang, Z. Zhang, Y. Zhang, A. Nie, W. Zhao, D. Wang, F. Huang, T. Zhai, *Adv. Mater.* **2020**, *32*, 2001979.
[43] D. Yang, X. Hu, M. Zhuang, Y. Ding, S. Zhou, A. Li, Y. Yu, H. Li, Z. Luo, L. Gan, T. Zhai, *Adv. Funct. Mater.* **2018**, *28*, 1800785.
[44] X. Wang, Y. Li, L. Huang, X. W. Jiang, L. Jiang, H. Dong, Z. Wei, J. Li, W. Hu, *J. Am. Chem. Soc.* **2017**, *139*, 14976.
[45] G. Qiu, Y. Du, A. Charnas, H. Zhou, S. Jin, Z. Luo, D. Y. Zemlyanov, X. Xu, G. J. Cheng, P. D. Ye, *Nano Lett.* **2016**, *16*, 7364.
[46] Yang, S. C. Liu, X. Wang, Z. Li, Y. Zhang, G. Zhang, D. J. Xue, J. S. Hu, *Adv. Funct. Mater.* **2019**, *29*, 1900411.
[47] L. Li, W. Wang, P. Gong, X. Zhu, B. Deng, X. Shi, G. Gao, H. Li, T. Zhai, *Adv. Mater.* **2018**, *30*, 1706771.
[48] L. Pi, C. Hu, W. Shen, L. Li, P. Luo, X. Hu, P. Chen, D. Li, Z. Li, X. Zhou, T. Zhai, *Adv. Funct. Mater.* **2020**, *30*, 2004375.
[49] S. R. Tamalampudi, Y. Y. Lu, R. K. U, R. Sankar, C. D. Liao, K. M. B , C. H. Cheng, F. C. Chou, Y. T. Chen, *Nano Lett.* **2014**, *14*, 2800.
[50] L. Li, W. Han, L. Pi, P. Niu, J. Han, C. Wang, B. Su, H. Li, J. Xiong, Y. Bando, T. Zhai, *InfoMat* **2019**, *1*, 54.
[51] J. K. Qin, F. C. Zhou, J. L. Wang, J. W. Chen, C. Wang, X. Y. Guo, S. X. Zhao, Y. Pei, L. Zhen, P. D. Ye, S. P. Lau, Y. Zhu, C. Y. Xu, Y. Chai, *ACS Nano* **2020**, *14*, 10018.
[52] T. Hong, B. Chamlagain, W. Lin, H. J. Chuang, M. H. Pan, Z. X. Zhou, Y. Q. Xu, *Nanoscale* **2014**, *6*, 8978.
[53] M. J. Dai, Z. G. Wang, F. K. Wang, Y. F. Qiu, J. Zhang, C. Y. Xu, T. Y. Zhai, W. W. Cao, Y. Q. Fu, D. C. Jia, Y. Zhou, P. A. Hu, *Nano Lett.* **2019**, *19*, 5410.